# Probe beam deflection technique with liquid immersion for fast mapping of thermal conductance [REE]



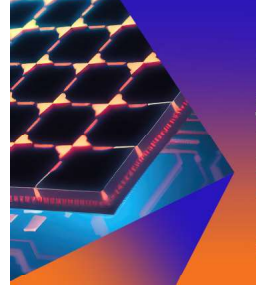
Appl. Phys. Lett. 124, 042201 (2024) https://doi.org/10.1063/5.0179581





CrossMark

25 January 2024 21:3



### **Applied Physics Letters**

Special Topic: Hybrid and Heterogeneous Integration in Photonics: From Physics to Device Applications

**Submit Today** 





# Probe beam deflection technique with liquid immersion for fast mapping of thermal conductance

Cite as: Appl. Phys. Lett. **124**, 042201 (2024); doi: 10.1063/5.0179581 Submitted: 3 October 2023 · Accepted: 3 January 2024 · Published Online: 22 January 2024







Jinchi Sun, <sup>1</sup> (1) Zhe Cheng, <sup>1,2</sup> (1) Jianbo Liang, <sup>3</sup> Naoteru Shigekawa, <sup>3</sup> (1) Keisuke Kawamura, <sup>4</sup> (1) Hiroki Uratani, <sup>4</sup> Yoshiki Sakaida, <sup>4</sup> and David G. Cahill <sup>1,a)</sup> (1)

#### **AFFILIATIONS**

- Department of Materials Science and Engineering and Materials Research Laboratory, University of Illinois at Urbana-Champaign, Urbana. Illinois 61801. USA
- $^2$ School of Integrated Circuits and Frontiers Science Center for Nano-optoelectronics, Peking University, Beijing 100871, China
- <sup>3</sup>Department of Physics and Electronics, Osaka Metropolitan University, Sugimoto 3-3-138, Sumiyoshi, Osaka 558-8585, Japan
- <sup>4</sup>SIC Division, Air Water Inc., 2290-1 Takibe, Toyoshina Azumino, Nagano 399-8204, Japan

#### **ABSTRACT**

Frequency-domain probe beam deflection (FD-PBD) is an experimental technique for measuring thermal properties that combines heating by a modulated pump laser and measurement of the temperature field via thermoelastic displacement of the sample surface. In the conventional implementation of FD-PBD, the data are mostly sensitive to the in-plane thermal diffusivity. We describe an extension of FD-PBD that introduces sensitivity to through-plane thermal conductance by immersing the sample in a dielectric liquid and measuring the beam deflection created by the temperature field of the liquid. We demonstrate the accuracy of the method by measuring (1) the thermal conductivity of a 310 nm thick thermally grown oxide on Si, (2) the thermal boundary conductance of bonded interface between a 3C-SiC film and a single crystal diamond substrate, and (3) the thermal conductivities of several bulk materials. We map the thermal boundary conductance of a 3C-SiC/diamond interface with a precision of 1% using a lock-in time constant of 3 ms and dwell time of 15 ms. The spatial resolution and maximum probing depth are proportional to the radius of the focused laser beams and can be varied over the range of 1–20  $\mu$ m and 4–80  $\mu$ m, respectively, by varying the  $1/e^2$  intensity radius of the focused laser beams from 2 to 40  $\mu$ m. FD-PBD with liquid immersion thus enables fast mapping of spatial variations in thermal boundary conductance of deeply buried interfaces.

Published under an exclusive license by AIP Publishing. https://doi.org/10.1063/5.0179581

Time-domain thermoreflectance (TDTR) and frequency-domain thermoreflectance (FDTR) are well-established techniques for mapping spatial variations of thermal transport coefficients, i.e., thermal conductivity<sup>1–7</sup> and thermal boundary conductance.<sup>3,8–10</sup> An ac temperature excursion at the surface of a sample is generated by a modulated pump laser and is detected via changes of the intensity of a reflected probe laser through the temperature dependence of the optical reflectivity. The small changes in the intensity of the probe laser are detected synchronously with the modulated pump laser using lock-in detection. A relatively long time constant of the lock-in amplifier is necessary to achieve a sufficient signal-to-noise ratio, and therefore, the rate of data acquisition in TDTR mapping experiments is typically limited to a few points per second.<sup>11</sup>

A high modulation frequency  $f>1\,\mathrm{MHz}$  is typically used in TDTR. Therefore, the maximum probing depth is small and

comparable to the penetration depth  $d_{th} = \sqrt{\Lambda/(\pi C f)}$ , where  $\Lambda$  is the thermal conductivity and C is the volumetric heat capacity. <sup>12</sup> At f=1 MHz,  $d_{th}$  ranges between 0.2  $\mu$ m for a typical polymer to 7  $\mu$ m for Au.

The temperature excursion can also be detected via the mirage effect, i.e., the deflection of the probe beam due to the thermally induced gradient of refractive index.<sup>13</sup> We have previously reported two variations of frequency-domain probe beam deflection technique (FD-PBD).<sup>14,15</sup> In FD-PBD, the temperature field in the sample created by a modulated pump laser beam is detected by the deflection of a probe laser beam. For most materials, FD-PBD has a larger signal-tonoise than FDTR and provides a larger probing depth than TDTR.

The original implementation of FD-PBD made use of the beam deflection by the temperature field in a transparent solid sample, e.g.,

a) Author to whom correspondence should be addressed: d-cahill@illinois.edu

an oxide glass or amorphous polymer. <sup>14,16</sup> The polymer is adhered to an Al-coated bulk silica substrate, and the pump and probe beams pass through the polymer sample. <sup>14</sup> The beam deflection is generated in the polymer due to the temperature dependence of the density and refractive index.

To extend FD-PBD to optically opaque materials, we developed a second version, where the beam deflection is generated by surface displacements generated by thermal expansion and is mostly sensitive to the in-plane thermal diffusivity. The thermal penetration depth is of the same order as the 1/e<sup>2</sup> intensity radius of the focused laser beam.

Here, we describe a third variation, liquid immersion probe beam deflection (LI-PBD), that provides good sensitivity to thermal conductance and fast data acquisition time. The Al-coated sample is immersed in a dielectric liquid with known thermal properties and thermo-optic coefficient. The thermal conductance can be extracted from magnitude of the beam deflection generated by the liquid; the signal-to-noise ratio is improved due to the large thermo-optic coefficient of the liquid.

The sample geometry is illustrated schematically in Fig. 1(a). The sample under study is first coated with a 50 nm-thick Al film using magnetron sputtering and then placed in a fused quartz cuvette filled with a transparent dielectric liquid (3M<sup>TM</sup> Novec<sup>TM</sup> 7500 Engineered Fluid,  $C_9H_5F_{15}O$ , hereinafter referred to as "liquid"). The properties of the liquid at room temperature are: thermal conductivity  $\Lambda_l = 0.065$  W/m-K, volumetric heat capacity  $C_l = 1.82$  MJ/m³-K (from datasheet of 3M<sup>TM</sup>), refractive index  $n_l = 1.29$ , <sup>17</sup> and thermo-optic coefficient  $\frac{dn_l}{dT} = -3.5 \times 10^{-4}$  K<sup>-1</sup> (see the supplementary material). The power of the incident pump laser is a square wave at modulation frequency f with an average of  $P_0$  and maximum of  $2P_0$ . The power of

the incident probe laser is a constant,  $P_1$ . Since the intensity of pump laser has a Gaussian profile, the ac temperature excursion created by the pump laser is not uniform and induces a radial gradient of the refractive index in the liquid. The probe laser beam has an offset from the pump beam; this offset is needed so that probe beam overlaps with the region of the sample with a large lateral temperature gradient. The magnitude of the deflection can be used to extract the thermal conductance of the sample by fitting a model, which was described previously  $^{16.18-20}$  and is briefly reviewed here.

We use a cylindrical coordinate system with the origin at the intersection of center of the pump beam and the liquid/Al interface and the z-axis and r-axis perpendicular and parallel to this interface, respectively. Hankel (r to k) and Fourier (t to  $\omega$ ) transforms are then performed to convert the heat diffusion equation to an algebraic expressions. The change of optical path length in the liquid is modeled as an effective surface displacement, <sup>18,19</sup>

$$\hat{Z}_l(k,\omega) = -\frac{1}{n_l} \frac{dn_l}{dT} \left( k^2 + \frac{i\omega C_l}{\Lambda_l} \right)^{-\frac{1}{2}} \hat{T}_{z=0}(k,\omega). \tag{1}$$

The expression for the surface temperature is 21,22

$$\hat{T}_{z=0}(k,\omega) = \frac{A_0}{2\pi} e^{-w_0^2 k^2/8} G_{tot}(k,\omega),$$
(2)

where  $w_0$  is the  $1/e^2$  radii of the focused pump beam and  $G_{tot}(k,\omega)$  is the overall thermal conductance of the layered structure liquid/Al/thin film/substrate, which is solved by a transfer matrix approach. The amplitude of the pump laser is

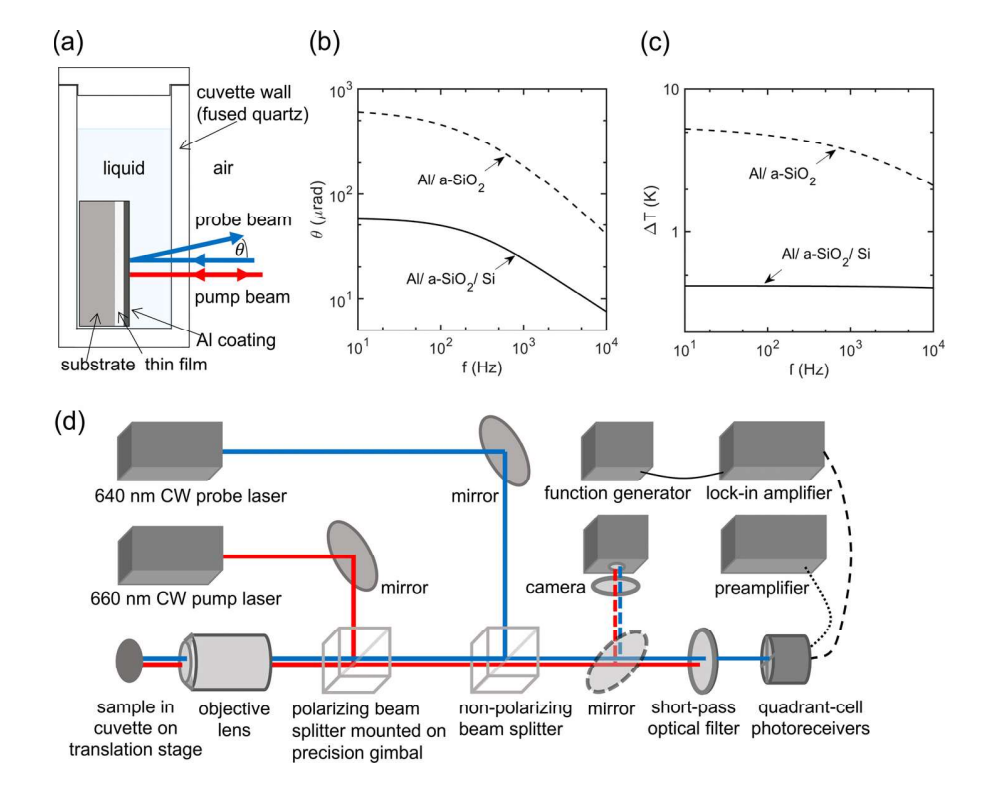


FIG. 1. (a) Schematic of the measurement geometry. (b) Calculated amplitude of PBD angle  $\theta$  and (c) calculated ac temperature excursion  $\Delta T$  for liquid/40 nm Al/ 310 nm a-SiO<sub>2</sub>/Si and liquid/40 nm Al/a- $SiO_2$  with pump power  $P_0 = 2$  mW, laser beam radii  $w_{\rm rms} = 8.4 \ \mu {\rm m}$ , and beam offset  $r_0 = 9.7 \ \mu \text{m}$ . (d) Schematic optical instrument. Black dashed, dotted, and solid lines represent the signal cables that transmit the up-down difference voltage of the photoreceiver, the sum voltage of the photoreceiver, and the reference signal from the function generator, respectively. The red and blue lines are the paths of the pump and probe beams, respectively.

$$A_0 = -\frac{4}{\pi} P_0 T_{a/q/l} A_{l/Al}, \tag{3}$$

where  $T_{a/q/l}$  is the transmittance of air/fused quartz/liquid and  $A_{l/Al}$  is the absorptance of the Al in the liquid. The PBD angle is 15

$$\widetilde{\theta} = \frac{C_1 n_l}{\pi n_a} \int_0^{+\infty} \hat{Z}_l(k, 2\pi f) e^{-w_1^2 k^2/8} (-J_1(kr_0)) k^2 dk, \tag{4}$$

where  $n_a$  is the refractive index of air,  $C_1$  a constant in the order of unity, f the modulation frequency of pump laser,  $w_1$  the  $1/e^2$  radii of the focused probe beam,  $J_1$  a Bessel function of first kind, and  $r_0$  the beam offset.  $\theta$  is a complex number that quantifies the response of the system to the primary cosine component of the pump laser. The counterpart in TDTR and FDTR is the surface temperature excursion.  $^{21,22}$ 

$$\widetilde{\Delta T} = \int_{0}^{+\infty} \hat{T}_{z=0}(k, 2\pi f) e^{-w_1^2 k^2/8} k dk.$$
 (5)

The pump and probe beam radii only appear in the form of  $w_0^2 + w_1^2$  and can be combined into  $w_{\rm rms} = \sqrt{(w_0^2 + w_1^2)/2}$ .

To compare the characteristics of PBD angle and surface temperature excursion, the magnitudes  $\theta = \mathrm{abs}(\widetilde{\theta})$  and  $\Delta T = \mathrm{abs}(\widetilde{\Delta T})$  are calculated for two reference samples: bulk fused silica (a-SiO<sub>2</sub>) and a 310 nm thick thermally grown a-SiO<sub>2</sub> layer on Si. Laser beam radii  $w_{\mathrm{rms}} = 8.4 \, \mu\mathrm{m}$  and beam offset  $r_0 = 9.7 \, \mu\mathrm{m}$  are used. As shown in Fig. 1(b), the frequency dependence of PBD angle  $\theta$ , i.e., the characteristic frequency, is nearly independent of the sample because it is determined by the thermal diffusivity of the liquid, laser beam radii, and beam offset. The magnitude of  $\theta$  varies with the sample because it also depends on the temperature excursion at the surface of the sample, which increases with decreasing thermal conductance of the sample. In contrast, the frequency dependence of  $\Delta T$ , i.e., the characteristic frequency, increases with the thermal diffusivity of the sample, see Fig. 1(c).

Figure 1(d) illustrates the measurement geometry. The pump laser and probe lasers are diode lasers operating at wavelengths of 660 and 640 nm, respectively. The laser beams are focused on the liquid/Al interface by an objective lens. When the reflected probe beam passes the objective lens, its deflection angle along the vertical direction is converted into displacement along the vertical direction and is measured by the quadrant-cell photoreceiver, <sup>15</sup>

$$\sqrt{8\pi} \frac{w_1}{\lambda_1} \theta = \sqrt{2} V_{amp} / V_{SUM}, \tag{6}$$

where  $\lambda_1$  is the wavelength of probe laser,  $V_{amp}$  the signal amplitude from the lock-in amplifier for the difference between signals of upper cells and lower cells of the photoreceiver, and  $V_{SUM}$  the sum of the signals of all cells of the photoreceiver.

The analysis of the measurement sensitivities is shown in Fig. 2 with the sensitivity of  $\theta$  to parameter x defined as

$$S_{\theta,x} = \frac{x}{\theta} \frac{d\theta}{dx}.$$
 (7)

The subscripts l, f, and s refer to properties of liquid, thin film, and substrate, respectively.  $G_1$  and  $G_2$  refer to the thermal boundary conductance of Al/thin film and thin film/substrate, respectively.

Figures 2(a) and 2(b) show results for a 310 nm thick thermally grown a-SiO<sub>2</sub> layer ( $\Lambda_f = 1.3 \, \text{W/m-K}$ ) on Si ( $\Lambda_s = 140 \, \text{W/m-K}$ ) with  $G_1 = G_2 = 100 \, \text{MW/m}^2$ -K.  $\theta$  is sensitive to the thermal conductance of the a-SiO<sub>2</sub> layer  $h_f/\Lambda_f$ , the thermal diffusivity of the liquid  $D_l = \Lambda_l/C_l$ , the laser beam radii  $w_{rms}$ , and the beam offset  $r_0$ . There is no sensitivity to heat capacity of solids because the temperature field in the solids is essentially in steady state at these frequencies. The thermal conductance of a thin film on a highly conductive substrate can be measured if the thermal conductance of the thin film is much smaller than that of the two interfaces.

Figures 2(c) and 2(d) show the sensitivities for 870 nm thick 3C-SiC ( $\Lambda_f$ =196 W/m-K) layer bonded to single crystal diamond ( $\Lambda_s$  = 2100 W/m-K) with  $G_1$  = 150 MW/m²-K and  $G_2$  = 23 MW/m²-K. The sensitivity to the thin film has contributions from both the thermal conductance in the through-thickness direction and the in-plane heat diffusion because of the high thermal conductivity of 3C-SiC. Because the thermal boundary conductance of 3C-SiC/diamond interface  $G_2$  is set to a small value in this example, the sensitivity to  $G_2$  is high. However, accurate measurement of  $G_2$  requires known  $G_1$  and  $\Lambda_f$  because their sensitivities are not negligible. It is generally impossible to determine more than one of  $G_1$ ,  $\Lambda_f$ , and  $G_2$  because they act in series. The possibility is determined by the sensitivity as shown in Fig. 2.

An important distinction of this liquid immersion PBD method in comparison with our previous work is the use of the amplitude of the signal. In previous FD-PBD techniques, we use a scaling factor and analyze only the frequency of dependence of the data.  $^{14,15}$  The liquid immersion method is, therefore, subject to additional uncertainties propagated from all proportional factors in the calculation of  $V_{amp}/V_{SUM}$  (including  $\frac{dm_l}{dT}$ ,  $T_{a/q/l}$ ,  $A_{l/Al}$ ,  $C_1$ , and  $w_1$ ). These uncertainties are removed by calibration as discussed in the supplementary material.

To demonstrate the accuracy of this technique, we measured several samples, see Table I. The thermal conductivity  $\Lambda_l$  and volumetric heat capacity  $C_l$  of the liquid are from the datasheet of 3M<sup>TM</sup>. The temperature is room temperature plus  $\Delta T_{ss} = \Delta T(f \to 0)$ . In a-SiO<sub>2</sub>/Si,  $\Lambda_s = 140 \, \text{W/m-K}$ ; in 3C-SiC/diamond,  $G_l = 150 \, \text{MW/m}^2\text{-K}$ ,  $\Lambda_f = 196 \, \text{W/m-K}$ ,  $\Lambda_s = 2100 \, \text{W/m-K}$ , which, along with film thicknesses, are obtained from TDTR. <sup>22–24</sup> The measured thermal conductivity of the thin films, thermal boundary conductance, and thermal conductivity of bulk materials agree well with reference values, with a deviation of approximately 10%.

To speed up the data acquisition in the mapping of thermal boundary conductance  $G_2$ , we optimize the beam offset  $r_0$  and modulation frequency f to minimize the uncertainty due to noise,

$$\delta G_2/G_2 = \frac{\delta \theta/\theta}{|S_{\theta,G_2}|},\tag{8}$$

where the noise  $\delta\theta/\theta$  equals the ratio of standard deviation and mean value of  $V_{\rm amp}/V_{\rm SUM}$  measured as a function of time. Figures 3(a) and 3(b) show  $\delta G_2/G_2$  for different combinations of  $r_0$  and f; we find that  $f=100\,{\rm Hz}$  and  $r_0=6.8\,\mu{\rm m}$  is optimal. As a rule of thumb, the optimal beam offset  $r_0$  can be found experimentally by adjusting the beam offset  $r_0$  until the signal  $\theta$  reaches the maximum value. At this maximum,  ${\rm d}\theta/{\rm d}r_0=0$ , and the signal noise  $\delta\theta$  caused by fluctuations of the beam offset  $\delta r_0$  approaches zero, which is, otherwise, the dominant source of noise. The beam offset can be optimized this way because it has

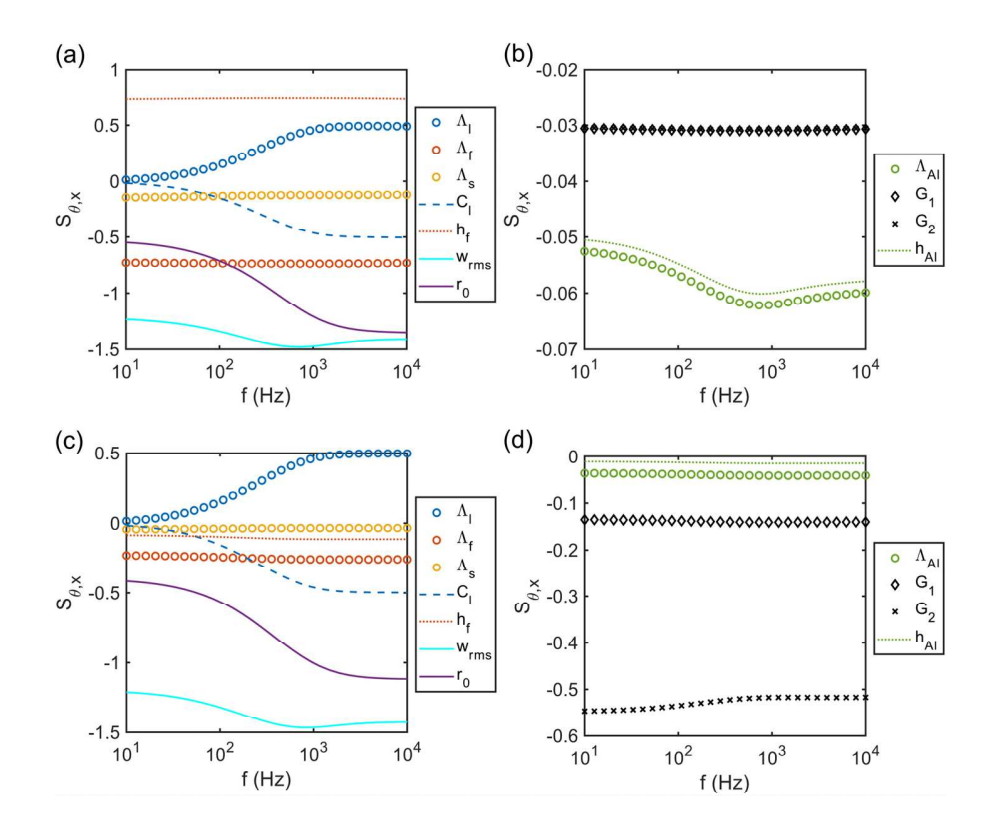


**FIG. 2.** Calculated sensitivities of the amplitude of the PBD angle  $\theta$  for (a) and (b) liquid/40 nm Al/310 nm a-SiO<sub>2</sub>/Si and for (c) and (d) liquid/98 nm Al/870 nm 3C-SiC/diamond.  $\Lambda$ , C, and h are the thermal conductivity, volumetric heat capacity, and thickness. The subscripts l, f, and s refer to liquid, thin film, and substrate.  $G_1$  and  $G_2$  are the thermal boundary conductance of the Al/thin-film interface and thin-film/ substrate interface. Laser beam radii  $W_{rms} = 8.4 \ \mu m$  and beam offset  $r_0 = 9.7 \ \mu m$ .

negligible influence on signal sensitivities to thermal properties. Figure 3(c) shows that the decrease in  $\delta G_2/G_2$  with increasing time constant of lock-in amplifier  $\tau$  roughly follows the expected scaling law  $\delta G_2/G_2 \propto \tau^{-0.5}$ . The signal-to-noise ratio can be enhanced by using a liquid with a higher figure-of-merit (FOM) (see the supplementary material).

The spatial resolution and maximum probing depth of the LI-PBD are proportional to the laser beam radii  $w_{\rm rms}$ . Figure 4(a) shows the exponential decay of sensitivity to thermal boundary conductance of buried interface  $|S_{\theta,G2}|$  with increasing depth  $h_f$  of the buried interface. We define  $d_1$  as the depth  $h_f$  at which  $|S_{\theta,G2}|$  decays by a factor of  $1/e^2$  relative to the maximum. With isotropic thermal conductivity, the

sensitivity also becomes negligible outside a region with a radius of  $d_1$ . Thus,  $d_1$  is also an estimate of the lateral spatial resolution. The sensitivity required to detect a 20% change of thermal boundary conductance is  $|S_{\theta,G^2}|=(\delta\theta/\theta)/(\delta G_2/G_2)=0.1\%/20\%=0.005$ . The thickness  $h_f$  at which  $|S_{\theta,G^2}|$  drops to 0.005, defined as  $d_2$ , is, thus, an estimate of the maximum probing depth. Figures 4(b) and 4(c) show that  $d_1\sim 0.6\,w_{\rm rms}$  (see the supplementary material for another way to estimate the spatial resolution) and  $d_2\sim 2\,w_{\rm rms}$  can be tuned from 1 to 20  $\mu{\rm m}$  and 4 to 80  $\mu{\rm m}$ , respectively, by varying  $w_{\rm rms}$  from 1.7 to 42  $\mu{\rm m}$ .

When the laser beam radii  $w_{\rm rms}$  is large compared to the thermal diffusion length in the liquid  $d_{th,l} = \sqrt{\Lambda_l/(\pi C_l f)}$ , the PBD angle  $\theta$ 

**TABLE I.** Measurement results with modulation frequency  $f=200\,\mathrm{Hz}$ , laser beam radii  $w_{\mathrm{rms}}=8.4\,\mu\mathrm{m}$ , and beam offset  $r_0=9.7\,\mu\mathrm{m}$ .

Sample	$P_0$ (mW)	$P_1$ (mW)	V <sub>SUM</sub> (V)	$V_{ m amp} \ ({ m mV})$	$\Delta T_{\rm ss}\left({ m K} ight)$	Measured material or interface	Measured value	Reference value	Error (%)
45 nm Al/a-SiO <sub>2</sub>	1.51	2.97	0.608	3.77	8.0	$a$ -SiO $_2$	1.31 W/m-K	1.31 W/m-K <sup>a</sup>	0
40 nm Al/310 nm a-SiO <sub>2</sub> /Si	12.1	2.97	0.614	3.78	1.5	$a$ -SiO $_2$	1.22 W/m-K	1.29 W/m-K <sup>a</sup>	-5
98 nm Al/870 nm 3C-SiC/diamond	49.8	2.97	0.605	4.95	1.1	3C-SiC/ diamond	29 MW/m <sup>2</sup> -K	$34 \mathrm{MW/m^2 - K^b}$	15
50 nm Al/SrTiO <sub>3</sub> (100) 45 nm Al/MgO (100)	6.04 24.2	2.97 2.97	0.608 0.612	3.42 2.84	2.2 1.3	SrTiO₃ MgO	9.65 W/m-K 54.0 W/m-K	11.0 W/m-K <sup>a</sup> 51.9 W/m-K <sup>a</sup>	$-12 \\ 4$

<sup>&</sup>lt;sup>a</sup>See https://cahill.matse.illinois.edu/software-and-data/; accessed 10 August 2023.

<sup>&</sup>lt;sup>b</sup>Measured using TDTR.

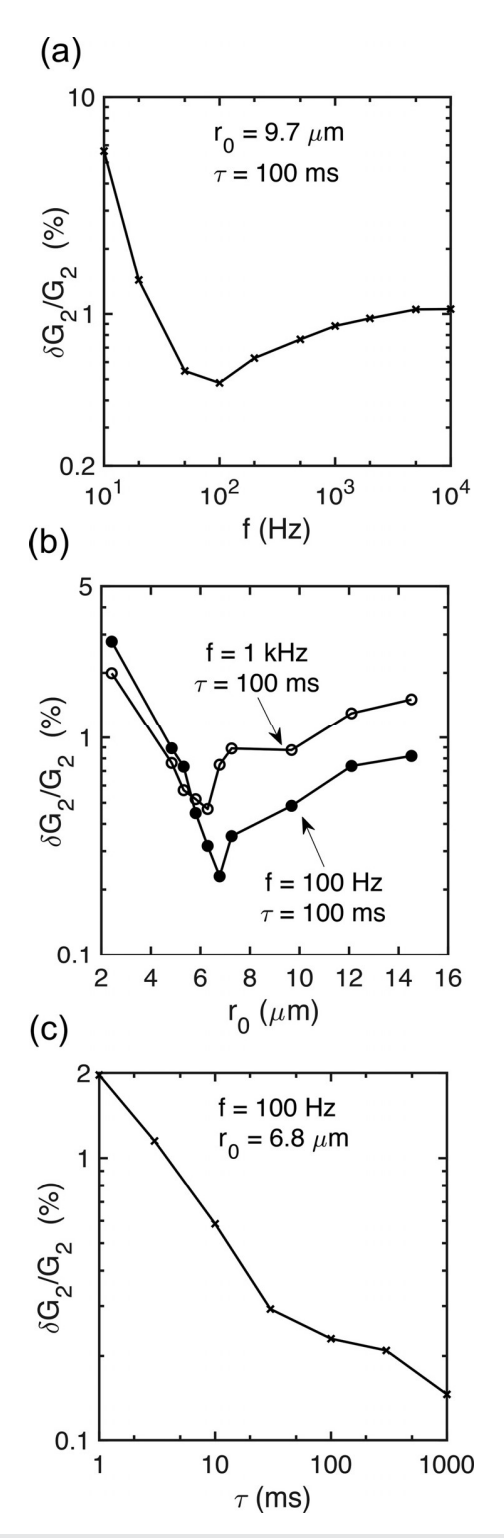


**FIG. 3.** Uncertainty of measured  $G_2$  in 98 nm Al/3C-SiC/diamond due to noise as a function of (a) modulation frequency f, (b) beam offset  $r_0$ , and (c) time constant of lock-in amplifier  $\tau$ . Laser beam radii  $w_{\rm rms}=8.4~\mu{\rm m}$ .

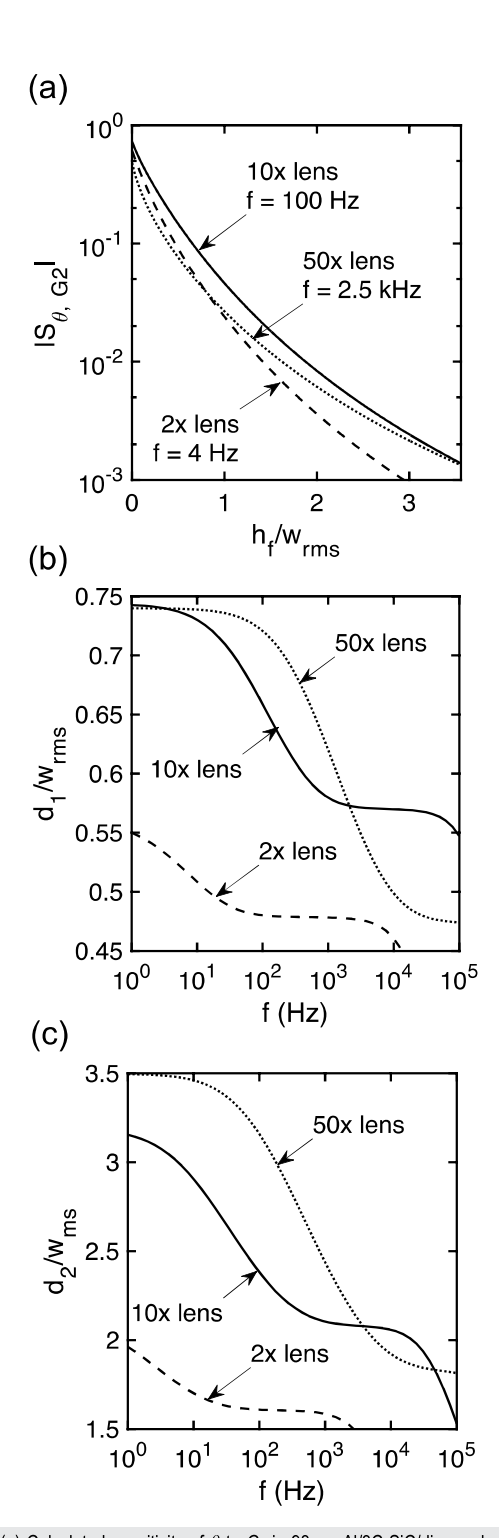


**FIG. 4.** (a) Calculated sensitivity of  $\theta$  to  $G_2$  in 98 nm Al/3C-SiC/diamond as a function of the depth of the buried interface  $h_h$  (b) calculated spatial resolution  $d_1$ ; and (c) calculated maximum probing depth  $d_2$ . Laser beam radii  $w_{\rm rms}=42$ , 8.4, and 1.7  $\mu{\rm m}$  for  $2\times$ ,  $10\times$ , and  $50\times$  objective lens, respectively. Beam offset  $r_0=0.80 w_{\rm rms}$ .

will scale with  $1/w_{\rm rms}$ , while the signal magnitude  $V_{\rm amp}$  will be independent of  $w_{\rm rms}$  if the surface temperature excursion  $\Delta T$  and frequency f are fixed. The pump power  $P_0$  needed to have  $\Delta T$  fixed will scale with  $w_{\rm rms}$  or  $\sqrt{w_{\rm rms}}$  if the thermal conduction is dominated by the substrate, or a thin film or interface, respectively.

To demonstrate the mapping capability, we mapped the thermal boundary conductance  $G_2$  in a sample of 870 nm thick 3C-SiC bonded to diamond over a 220  $\times$  50  $\mu$ m<sup>2</sup> area with  $w_{\rm rms} = 8.4 \,\mu$ m,  $f = 100 \,\rm Hz$ ,  $r_0 = 6.8 \,\mu\text{m}$ , and  $\tau = 3 \,\text{ms}$ . The sample is moved by the translation stage at a step size of  $5 \mu m$ . After moving to a new location, data are acquired after waiting for a dwell time of  $5\,\tau = 15\,\text{ms}$ . As shown in Fig. 3(c), the uncertainty of measured  $G_2$  due to noise is approximately 1%. A dwell time of  $\tau$  is usually sufficient, reducing the total data acquisition time to 1.3s for this  $44 \times 5$  mapping, which would take thermoreflectance based technique more than ten times as long. The mapping of  $G_2$  is shown in Fig. 5(a), and a bright field optical image of the same region is shown in Fig. 5(b). G2 has a mean value of 30 MW/m<sup>2</sup>-K and spatial variation of 40%, indicating nonuniformity of bonding. This mapping reveals strip-shaped regions with length scale of tens of micrometer, where  $G_2$  is reduced, and a  $10 \times 10 \,\mu\text{m}^2$ region with  $G_2$  as small as  $10 \,\mathrm{MW/m^2}$ -K. These variations in the bonded interface are not revealed by optical imaging.

In summary, we demonstrate measurements and fast mapping of thermal conductance by a liquid immersion probe beam deflection (LI-PBD). The measured thermal conductivity of thin film, thermal boundary conductance of buried interface, and thermal conductivity of bulk materials are found to agree with reference values to within 10%. The time constant needed to achieve 1% noise-induced uncertainty in the mapping of the thermal boundary conductance of 3C-SiC/diamond interface is reduced to 3 ms, demonstrating fast detection of defects at the bonded interface. The spatial resolution and maximum probing depth are estimated to be tunable over the range of 1–20  $\mu \rm m$  and 4–80  $\mu \rm m$ , respectively, by varying the size of the focused laser spot over the range of 1.7–42  $\mu \rm m$ . Compared to steady-state thermoreflectance,  $^{25}$  LI-PBD has the advantage of higher signal-to-noise ratio and relaxed requirements on the smoothness of the sample surface.



**FIG. 5.** (a) Mapping of the thermal boundary conductance  $G_2$  in 98 nm Al/870 nm 3C-SiC/single crystal diamond sample; (b) optical microscope image of the same region. Modulation frequency f=100 Hz, laser beam radii  $w_{\rm rms}=8.4~\mu{\rm m}$ , beam offset  $r_0=6.8~\mu{\rm m}$ , lock-in time constant  $\tau=3~{\rm ms}$ , dwell time = 15 ms, step size = 5  $\mu{\rm m}$ , pump power  $P_0=50~{\rm mW}$ , and probe power  $P_1=3.0~{\rm mW}$ .

See the supplementary material for the details of calibration for calculation of  $V_{amp}/V_{SUM}$  and the data of the correction factor for different beam offset and a formula of the model for data analysis incorporating the calibration (Sec. 1); the figure-of-merit (FOM) of the liquid for enhancing signal-to-noise ratio and another liquid with higher FOM (Sec. 2); and a different way of estimating the spatial resolution, which is based on calculation of the spatial distribution of the local contribution to the signal, and that the result agrees well with what we get in this paper (Sec. 3).

This research was supported by the NSF through the University of Illinois at Urbana-Champaign Materials Research Science and Engineering Center No. DMR-1720633.

## AUTHOR DECLARATIONS Conflict of Interest

David G. Cahill and Jinchi Sun have filed two provisional patent applications for this work.

#### **Author Contributions**

Jinchi Sun: Conceptualization (equal); Data curation (equal); Formal analysis (equal); Investigation (equal); Methodology (equal); Software (equal); Validation (equal); Visualization (equal); Writing - original draft (equal); Writing - review & editing (equal). Zhe Cheng: Data curation (supporting); Formal analysis (supporting); Investigation (supporting); Writing - review & editing (supporting). Jianbo Liang: Investigation (supporting); Resources (supporting). Naoteru Shigekawa: Investigation (supporting); Resources (supporting). Keisuke Kawamura: Investigation (supporting); Resources (supporting). Hiroki Uratani: Investigation (supporting); Resources (supporting). Yoshiki Sakaida: Investigation (supporting); Resources (supporting). David G. Cahill: Conceptualization (equal); Data curation (equal); Formal analysis (equal); Funding acquisition (equal); Investigation (equal); Methodology (equal); Project administration (equal); Resources (equal); Supervision (equal); Writing - original draft (equal); Writing - review & editing (equal).

#### **DATA AVAILABILITY**

The data that support the findings of this study are available from the corresponding author upon reasonable request.

#### **REFERENCES**

- <sup>1</sup>S. Huxtable, D. G. Cahill, V. Fauconnier, J. O. White, and J.-C. Zhao, "Thermal conductivity imaging at micrometre-scale resolution for combinatorial studies of materials," Nat. Mater. 3(5), 298–301 (2004).
- <sup>2</sup>E. López-Honorato, C. Chiritescu, P. Xiao, D. G. Cahill, G. Marsh, and T. J. Abram, "Thermal conductivity mapping of pyrolytic carbon and silicon carbide coatings on simulated fuel particles by time-domain thermoreflectance," J. Nucl. Mater. 378(1), 35–39 (2008).
- <sup>3</sup>J. Yang, C. Maragliano, and A. J. Schmidt, "Thermal property microscopy with frequency domain thermoreflectance," Rev. Sci. Instrum. **84**(10), 104904 (2013).
- <sup>4</sup>A. Sood, R. Cheaito, T. Bai, H. Kwon, Y. Wang, C. Li, L. Yates, T. Bougher, S. Graham, and M. Asheghi, "Direct visualization of thermal conductivity suppression due to enhanced phonon scattering near individual grain boundaries," Nano Lett. 18(6), 3466–3472 (2018).

- <sup>5</sup>Z. Cheng, R. Cheaito, T. Bai, L. Yates, A. Sood, B. M. Foley, T. L. Bougher, F. Faili, M. Asheghi, and K. E. Goodson, *International Heat Transfer Conference Digital Library* (Begel House Inc., 2018).
- <sup>6</sup>D. H. Olson, J. L. Braun, and P. E. Hopkins, "Spatially resolved thermoreflectance techniques for thermal conductivity measurements from the nanoscale to the mesoscale," J. Appl. Phys. 126(15), 150901 (2019).
- <sup>7</sup>E. K. Pek, J. Brethauer, and D. G. Cahill, "High spatial resolution thermal conductivity mapping of SiC/SiC composites," J. Nucl. Mater. **542**, 152519 (2020).
- <sup>8</sup>D. B. Brown, W. Shen, X. Li, K. Xiao, D. B. Geohegan, and S. Kumar, "Spatial mapping of thermal boundary conductance at metal–molybdenum diselenide interfaces," ACS Appl. Mater. Interfaces 11(15), 14418–14426 (2019).
- <sup>9</sup>Z. Cheng, F. Mu, X. Ji, T. You, W. Xu, T. Suga, X. Ou, D. G. Cahill, and S. Graham, "Thermal visualization of buried interfaces enabled by ratio signal and steady-state heating of time-domain thermoreflectance," ACS Appl. Mater. Interfaces 13(27), 31843–31851 (2021).
- <sup>10</sup>J. Yang, E. Ziade, C. Maragliano, R. Crowder, X. Wang, M. Stefancich, M. Chiesa, A. K. Swan, and A. J. Schmidt, "Thermal conductance imaging of graphene contacts," J. Appl. Phys. 116(2), 023515 (2014).
- <sup>11</sup>X. Ji, Z. Cheng, E. K. Pek, and D. G. Cahill, "Thermal conductivity mapping of oxidized SiC/SiC composites by time-domain thermoreflectance with heterodyne detection," J. Am. Ceram. Soc. 104(9), 4773–4781 (2021).
- <sup>12</sup>p. Jiang, X. Qian, and R. Yang, "Tutorial: Time-domain thermoreflectance (TDTR) for thermal property characterization of bulk and thin film materials," J. Appl. Phys. 124(16), 161103 (2018).
- <sup>13</sup>M. Bertolotti and R. L. Voti, "A note on the history of photoacoustic, thermal lensing, and photothermal deflection techniques," J. Appl. Phys. 128(23), 230901 (2020).
- <sup>14</sup>G. Lv, E. Jensen, C. Shen, K. Yang, C. M. Evans, and D. G. Cahill, "Effect of amine hardener molecular structure on the thermal conductivity of epoxy resins," ACS Appl. Polym. Mater. 3(1), 259–267 (2020).
- <sup>15</sup>J. Sun, G. Lv, and D. G. Cahill, "Frequency-domain probe beam deflection method for measurement of thermal conductivity of materials on micron length scale," Rev. Sci. Instrum. 94(1), 014903 (2023).

- <sup>16</sup>J. Shin, J. Sung, M. Kang, X. Xie, B. Lee, K. M. Lee, T. J. White, C. Leal, N. R. Sottos, and P. V. Braun, "Light-triggered thermal conductivity switching in azobenzene polymers," Proc. Natl. Acad. Sci. U. S. A. 116(13), 5973–5978 (2019).
- <sup>17</sup>S. K. Y. Tang, Z. Li, A. R. Abate, J. J. Agresti, D. A. Weitz, D. Psaltis, and G. M. Whitesides, "A multi-color fast-switching microfluidic droplet dye laser," Lab Chip 9(19), 2767–2771 (2009).
- <sup>18</sup>X. Zheng, D. G. Cahill, R. Weaver, and J.-C. Zhao, "Micron-scale measurements of the coefficient of thermal expansion by time-domain probe beam deflection," J. Appl. Phys. 104(7), 073509 (2008).
- <sup>19</sup>X. Xie, X. Zheng, R. Weaver, J.-C. Zhao, and D. G. Cahill, "Erratum: 'Micronscale measurements of the coefficient of thermal expansion by time-domain probe beam deflection' [J. Appl. Phys. 104, 073509 (2008)]," J. Appl. Phys. 122(21), 219901 (2017).
- 20 X. Xie, J. M. Dennison, J. Shin, Z. Diao, and D. G. Cahill, "Measurement of water vapor diffusion in nanoscale polymer films by frequency-domain probe beam deflection," Rev. Sci. Instrum. 89(10), 104904 (2018).
- <sup>21</sup>A. J. Schmidt, R. Cheaito, and M. Chiesa, "A frequency-domain thermoreflectance method for the characterization of thermal properties," Rev. Sci. Instrum. **80**(9), 094901 (2009).
- <sup>22</sup>D. G. Cahill, "Analysis of heat flow in layered structures for time-domain thermoreflectance." Rev. Sci. Instrum. 75(12), 5119–5122 (2004).
- <sup>23</sup>K. Kang, Y. K. Koh, C. Chiritescu, X. Zheng, and D. G. Cahill, "Two-tint pump-probe measurements using a femtosecond laser oscillator and sharp-edged optical filters," Rev. Sci. Instrum. 79(11), 114901 (2008).
- <sup>24</sup>G. T. Hohensee, W.-P. Hsieh, M. D. Losego, and D. G. Cahill, "Interpreting picosecond acoustics in the case of low interface stiffness," Rev. Sci. Instrum. 83(11), 114902 (2012).
- <sup>25</sup>M. S. Bin Hoque, Y. R. Koh, K. Aryana, E. R. Hoglund, J. L. Braun, D. H. Olson, J. T. Gaskins, H. Ahmad, M. M. M. Elahi, and J. K. Hite, "Thermal conductivity measurements of sub-surface buried substrates by steady-state thermoreflectance," Rev. Sci. Instrum. 92(6), 064906 (2021).